AD A105184

FOREIGN TECHNOLOGY DIVISION
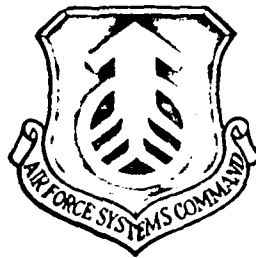
ACTA MECHANICA SINICA

(Selected Articles)

DTIC
SELECTED
OCT 8 1981

A

81 10 7 164

FTD-ID(RS)T-0704-81

EDITED TRANSLATION

FTD-ID(RS)T-0704-81

11 September 1981

MICROFICHE NR: FTD-81-C-000839

ACTA MECHANICA SINICA (Selected Articles)

English pages: 44

Edited trans, of

Source: Acta Mechanica Sinica, Nr. 1, 1979,
pp. 42-49, 70-73
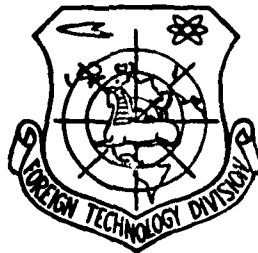
Country of origin: China
Translated by: SCITRAN
F33657-78-D-0619
Requester: FTD/TQTA
Approved for public release; distribution
unlimited.

FTD-ID(RS)T-0704-81

Date 11 Sep 19 81

TABLE OF CONTENTS

The Arbitrary Quasi-Orthogonal Surface Method for
Computing Three-Dimensional Flow in Turbine Machinery*

II.   Calculation of the Three-Dimensional Flow
With the S_1-surface Twisted

Xin Xiao-Kang   Jiang Jin-liang   Zhu Shi-can
(Fudan University)

Abstract

On the basis of the quasi-orthogonal
surface method, this paper obtains a three-
dimensional flow field solution of inviscous
fluids in turbine machinery. This method,
under the condition allowed by the storage of
the computer, can calculate any shapes of S_1
and S_2 surfaces (including twisting S_1 -
surfaces) and obtain the shapes of space stream-
lines and the three-dimensional distribution
of parameters such as velocity. The calcula-
tions for the two conditions of a centrifugal
compressor with a small impeller (ϕ110) indi-
cate the relative value of the twist of the S_1-
surface is about 3 - 10%. The S_1-surface
shows a double twist like a twist drill from
the inlet to the outlet.

Under the assumptions that the fluid is incompressible,
inviscous, and absolutely non-rotational, Reference [2] used
a binary solution superposition method to calculate the results
with twisted S_1 and S_2 surfaces. But because the turbine was
not real, the results can only be used as a qualitative refer-
ence. On the basis of quasi-orthogonal surface method, this
paper eliminates the assumption that the S_1 surface is a revolv-
ing body. In the processes of integration and the interpolation

1

by equal difference of flux, an equi-parameter transformation
is introduced to transform the flow region on the equi-ortho-
gonal surfaces to a rectangular region on the (ξ, η) plane.
It is then possible to use the procedures listed in Reference
[1] and various modification procedures to obtain the iterative
solution of the entire three-dimensional flow field. In the
search for the reverse transformation of the equi-parameter
transformation, this paper simultaneously offers three numeri-
cal methods (see Section III). The numerical calculation indi-
cates that the accuracy is very good in the reverse transforma-
tion using a straight line quadrangle instead of the curved
quadrangle. It is an approximation method which drastically
reduces the calculation time. Using this method a computer
program has been compiled for a centrifugal turbine and a cal-
culation has been carried out on the modified centrifugal com-
pressor turbine of the GJ11# pressure riser of Shanghai Diesel
Engine Factory. The calculated results indicate the twist of
the S_1 surface is relatively small. Therefore, it frequently
uses the S_1 surface to carry out the calculation for the revolv-
ing body assumption as a fairly good approximation. The S_1
surface, in addition, shows a double twists like a twist drill
from the inlet to the outlet. This method, in principle, is
applicable to any type of turbines. However, for axial flow
machinery we must add inlet and outlet corrections. The work
in this area is currently in progress.

I. Basic Assumption and Solution to the
     Velocity Gradient Equation

This paper uses two basic assumptions: 1. The working
medium (or fluid) is an inviscous, equi-C_p, and equi-C_v perfect
gas. The flow may be unisoentropic. However, for ease of
description, the entropy gradient term is neglected from the
equation. The friction loss of the real gases is reflected by

2

the variation process same as the one used in Reference [1].
2. The flow passing through the turbine is a constant relative
to the turbine. The kinetic equations are written in a rela-
tive cylindrical coordinate system (r, θ, z) .

The basic equations used in this work still are equations
(1) and (2) in Reference [1]. Here we slightly modify these
equations and rewrite them as

$$\frac{dW}{dq} = AW + B + \frac{1}{W}\left(\frac{dh_i'}{dq} - \omega\,\frac{d\lambda}{dq}\right) \tag{1}$$

where

$$
\left.
\begin{aligned}
A &= \frac{\cos^2\beta\left(\cos\alpha\,\dfrac{dr}{dq} - \sin\alpha\,\dfrac{dz}{dq}\right)}{r_c} - \frac{\sin^2\beta\,\dfrac{dr}{dq}}{r} + \sin\alpha\sin\beta\cos\beta\,\frac{d\theta}{dq} \\
B &= \left(\frac{dr}{dq}\sin\alpha + \frac{dz}{dq}\cos\alpha\right)\cos\beta\,\frac{dW_m}{dm} - 2\omega\sin\beta\,\frac{dr}{dq} \\
&\quad + r\cos\beta\left(\frac{dW_\theta}{dm} + 2\omega\sin\alpha\right)\frac{d\theta}{dq}
\end{aligned}
\right\} \tag{2}
$$

On the quasi-orthogonal surfaces, two independent varia-
bles q_m and θ are introduced as in Reference [1]. Therefore,
in the quasi-orthogonal surface of the single blade channel on
the (θ, q_m) plane (it is the region between the pressure sur-
face of one blade to the suction surface of another blade) the
flow field is shown approximately in Figure 1. The intersection
between S_2 surface and the quasi-orthogonal surface is indicated
as the dotted line. The intersection of the S_1 surface and the
quasi-orthogonal surface is shown as the point-solid line.
If the problem we are solving has $N + 1$ S_1 surfaces and $H + 1$
S_2 surfaces, then the equations of the intersection between the
quasi-orthogonal surfaces and the S_2 surfaces can be written as

$$\theta = f_k(q_m) \quad (k = 1, 2, \cdots, H + 1) \tag{3}$$

3

The intersection equations of the quasi-orthogonal surfaces and the S_1 surfaces can be written as

$$q_m = g_j(\theta) \quad (j = 1, 2, \cdots, N + 1) \tag{4}$$

Obviously, when $g_j(\theta) = $ const, it is the situation that S_1 surface is a revolving surface.

The first few steps of the problem solving procedure used in this paper are similar to those used in Reference [1]. Steps 1 - 5 are basically identical to those in Reference [1]. The only thing is that the coordinates (r_p, θ_p, z_p) of an arbitrary lattice point p (it is the intersecting point between S_1 surfaces, S_2 surfaces and the quasi-orthogonal surfaces) on the streamline should be a three-dimensional numerical set and it is no longer a two dimensional numerical set as in Reference [1]. Similarly, α, β, r_c , etc. are also presently a three-dimensional numerical set.
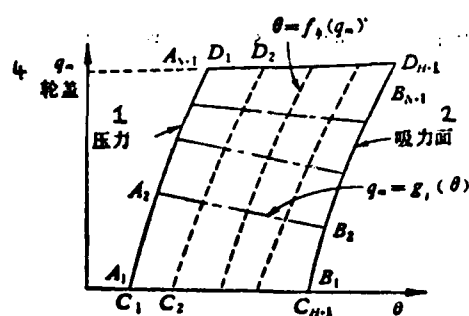

Figure 1. Key: 1. Pressure, 2. Suction surface, 4. Rotating cover.

With respect to setp 6 in Reference [1], we carry out the following modification. In order to make point p or the stream-line satisfy equation (1) simultaneously in both the q_m and the

4

θ directions, the following modification is made in solving
for the velocity gradient equation as proposed in Reference
[1]. Assuming that the value W at point A in Figure 2 is
known, then we first proceed with a numerical liner integration
along AB to find out the W value of all the points along AB.
We further perform integration along the intersecting line
with the S_1 surface to obtain the W value at all the lattice
points (Figure 2a). We shall designate them as the $W_1[j,k]$
numerical set. On the other hand, let us start from point A
to integrate linearly along AC in order to obtain the W value
of all points along AC and then integrate along the inter-
secting line with the S_2 surface. The obtained W values at
all the lattice points are designted as the $W_2[j,k]$ numerical
set. Finally, let
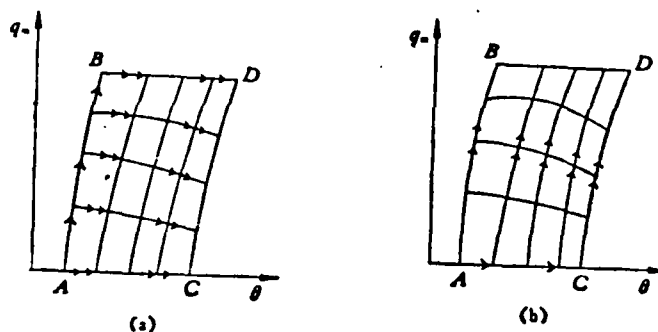
Figure 2

us take

$$W[j,k] = \frac{W_1[j,k] + W_2[j,k]}{2} \quad \left(\begin{matrix} j = 1, 2, \cdots, N+1 \\ k = 1, 2, \cdots, H+1 \end{matrix} \right)$$

as the relative velocity values of all the lattice points on
the quasi-orthogonal surfaces. The mathematical meaning of
this process is to make any point P simultaneously satisfy
equation (1) in two directions under the "average" idea described
above. In addition, we also use the numerical method which
starts from the center of the flow field toward the perimeter

to seek for solution. In this method the original starting point A is moved to the center of the flow field E (Figure 3). This would further raise the accuracy of the numerical solution.
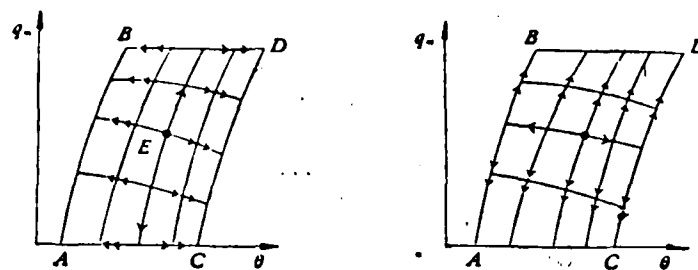
Figure 3

II. Flux Integration and Equi-Parameter Transformation

The major difficulty brought about by the elimination of the assumption that the S_1 surface is a revolving surface is how to carry out steps 8 and 9 used in Reference [1]. From Reference [1], it is known that the mass flux equation in the channel between two neighboring bladesthrough any quasi-orthogonal surface is

$$G = \iint_s \rho g W_m \cos(\psi - \alpha) r \, d\theta \, dq_m \tag{5}$$

where the integration region 5 is the ABCD region on the quasi-orthogonal surface (Figure 2). Since the S_1 surface is not a solving surface, the integral of equation (5) can no longer be written as a quadratic integration (i.e. integration first with respect to θ and then to q_m) as in Reference [1]. It must be written as a double integral as in equation (5). However, there is certain difficulty in the direct integration as in equation (5). For that, we have to introduce an equi-parameter transformation which transforms the ABCD region on

6

the quasi-orthogonal surface into a rectangular region on a certain transformation plane — (ξ, η) plane and also simultaneously transform every curved quadrangles regions surrounded by the intersections of S_1 and S_2 surfaces into rectangular region. Thus, the regions on the (ξ, η) plane become very regular. The intersection line of the S_1 surface is transformed into the η = const straight line and the intersection line of the S_2 surface is transformed into the ξ = const straight line. Therefore, the integrations in equation (5) become much easier on the (ξ, η) plane.

The following is the derivation of the equi-parameter transformation equations. Let us assume that there is a region ABCD surrounded by a curved quadrangle (Figure 4a) and the equations for the four sides are assumed as:

$$AC: q_m = q_i(\theta), \quad BD: q_m = q_{i+1}(\theta) \left.\vphantom{\begin{matrix}a\\b\end{matrix}}\right\} $$
$$AB: \theta = f_k(q_m), \quad CD: \theta = f_{k+1}(q_m) \qquad (6)$$

We are seeking for a transformation which transforms the curved quadrangle ABCD into the rectangle A*B*C*D* on the (ξ, η) plane (Figure 4b) and make

$$A^*C^*: \eta = \eta_i, \quad B^*D^*: \eta = \eta_{i+1} \left.\vphantom{\begin{matrix}a\\b\end{matrix}}\right\}$$
$$A^*B^*: \xi = \xi_k, \quad C^*D^*: \xi = \xi_{k+1} \qquad (7)$$

We found that the equi-parameter transformation below can achieve the above objectives:

$$\frac{\xi - \xi_k}{\xi_{k+1} - \xi_k} = \frac{\theta - f_k(q_m)}{f_{k+1}(q_m) - f_k(q_m)}, \quad f_k(q_m) < \theta \leqslant f_{k+1}(q_m) \left.\vphantom{\begin{matrix}a\\b\end{matrix}}\right\}$$
$$\frac{\eta - \eta_i}{\eta_{i+1} - \eta_i} = \frac{q_m - g_i(\theta)}{g_{i+1}(\theta) - g_i(\theta)}, \quad g_i(\theta) < q_m \leqslant g_{i+1}(\theta) \qquad (8)$$

7

For convenience, we can simplify equation (θ) as

$$\xi = \xi(\theta, q_m), \quad \eta = \eta(\theta, q_m) \tag{9}$$
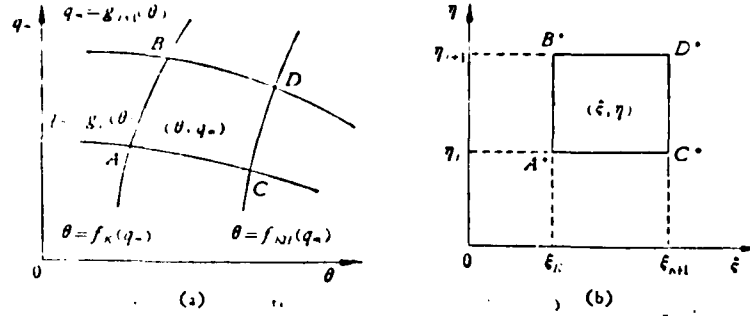
Figure 4

It is easy to write the Jacobi determinant which transforms equation (9) as

$$J = \frac{D(\xi, \eta)}{D(\theta, q_m)} = \begin{vmatrix} \dfrac{\partial \xi}{\partial \theta} & \dfrac{\partial \xi}{\partial q_m} \\ \dfrac{\partial \eta}{\partial \theta} & \dfrac{\partial \eta}{\partial q_m} \end{vmatrix} = \frac{\partial \xi}{\partial \theta} \frac{\partial \eta}{\partial q_m} - \frac{\partial \xi}{\partial q_m} \frac{\partial \eta}{\partial \theta} \tag{10}$$

Therefore, the flux integral (5) can be transformed into

$$G = \iint_s CK(\theta, q_m) d\theta dq_m = \iint_{s^*} CK(\xi, \eta) \frac{1}{|J|} d\xi d\eta \tag{11}$$

where

$$CK(\theta, q_m) = \rho g W_m \cos(\alpha - \psi) r.$$

If we take S* as a unit square area, then equation (11) can be written in the quadratic integral form:

$$G = \int_0^1 d\xi \int_0^1 CK(\xi, \eta) \frac{1}{|J|} d\eta = \int_0^1 d\eta \int_0^1 CK(\xi, \eta) \frac{1}{|J|} d\xi \tag{12}$$

8

Here the value of the Jacobi equation /J/ at the lattice point $(\theta_{l,k}, q_{m,k})$ is

$$\frac{1}{|J|} = \frac{[f_{l,k}(q_{m,k}) - \theta_{l,k}][g_{l,k}(\theta_{l,k}) - q_{m,k}]}{[1 - f'_k(q_{m,k}) \cdot g'_l(\theta_{l,k})] \Delta \xi \Delta \eta} \tag{13}$$

where $\quad \Delta \xi = \xi_{l+1} - \xi_l = 1/H, \ \Delta \eta = \eta_{l+1} - \eta_l = 1/N.$

Using this quadratic numerical calculation, we can obtain the calculated flux value. In order not to treat the coordinates "specially", from now on in all our procedures we will use the "average" method as we did in solving the velocity gradient equation. For example, in determining the flux, we let

$$G_1 = \int_0^1 d\eta \int_0^1 CK(\xi, \eta) \frac{1}{|J|} d\xi \tag{14}$$

$$G_2 = \int_0^1 d\xi \int_0^1 CK(\xi, \eta) \frac{1}{|J|} d\eta \tag{15}$$

then the calculate flux

$$G = (G_1 + G_2)/2 \tag{16}$$

Compare G with the given fixed flux G_O, if $\ |G - G_0|/G_0 < \varepsilon_G \ $, then switch to step 8. Otherwise use the method similar to the one used in Reference [1] to correct the velocity value at point A or E and repeat steps 6 and 7.

III. Flux Interpolation by Equal Difference and the Reverse Transformation

For step 8, which is the step using the interpolation by equal difference method to obtain the new coordinate positions of the streamline, we carry it out on the (ξ, η) plane. Because the integral is the quadratic integral form, therefore we can proceed using the same method as in Reference [1]. First we

9

obtain a set of new streamline coordinates $(\xi_{Gi}, \eta_{Gi})_{i,k}$ from
equation (4) and then we obtain another set of new streamline
coordinates (ξ_{G2}, η_{G2}) from equation (15). After taking their
average value, we get the new positions of the streamline
coordinate points from the interpolation by equal difference
in flux

$$\xi_G = (\xi_{G1} + \xi_{G2})/2, \quad \eta_G = (\eta_{G1} + \eta_{G2})/2 \tag{17}$$

The next problem is how to find θ_G and q_{mG} on the
physical plane (from q_{mG} we can get r_G and z_G) once the new
streamline coordinate positions ξ_G and η_G are found.

From the equi-parameter transformation (8), we know that
it is pretty difficult to find θ_G and q_{mG} from ξ_G and η_G. It
is because the real analytical solutions of $g_i(\theta)$ and $f_k(q_m)$
are actually not known. We have used various methods to look
for the reverse transformation. Here we are only going to dis-
cuss and compare three methods which we have used to conduct
detailed calculations.

1. Rigorous and "accurate" Reverse Transformation.
From the equi-parameter transformation (8), we know that when
$\xi_k < \xi_G \leqslant \xi_{k+1}$ and $\eta_i < \eta_G \leqslant \eta_{i+1}$

$$\left.\begin{array}{l} \xi_G = \dfrac{\xi_G - \xi_k}{\xi_{k+1} - \xi_k} = \dfrac{\theta - f_k(q_m)}{f_{k+1}(q_m) - f_k(q_m)} \\[2mm] \eta_G = \dfrac{\eta_G - \eta_i}{\eta_{i+1} - \eta_i} = \dfrac{q_m - g_i(\theta)}{g_{i+1}(\theta) - g_i(\theta)} \end{array}\right\} \tag{18}$$

Our purpose is to locate the θ_G and q_{mG} which satisfy
equation (18). For that, we are rewriting equation (18) as

$$\left.\begin{array}{l} \theta = f_k(q_m) + \xi_G[f_{k+1}(q_m) - f_k(q_m)] \\[2mm] q_m = g_i(\theta) + \eta_G[g_{i+1}(\theta) - g_i(\theta)] \end{array}\right\} \tag{19}$$

10

If an initial value $q_m^{(0)}$ is given by an approximation method, then we can use the following iteration method to obtain the iterative values of θ and q_m:

$$\left.\begin{aligned}
\theta^{(n)} &= f_k(q_m^{(n)}) + \xi_0[f_{k+1}(q_m^{(n)}) - f_k(q_m^{(n)})] \\
q_m^{(n+1)} &= g_l(\theta^{(n)}) + \eta_0[g_{l+1}(\theta^{(n)}) - g_l(\theta^{(n)})]
\end{aligned}\right\} \qquad (20)$$

Iteration stops when $|q_m^{(n+1)} - q_m^{(n)}| < \varepsilon_0$. Thus the reverse transformation which is "accurate" in the sense of approximation in numerical value is obtained.

2.   The Reverse Transformation Using the Linear Quad-
      Rangle Approximation.

Because it is time consuming to use the above equations, the reverse transformation which replaces the curved quadrangle by the linear quadrangle is proposed. It is obvious that, with increasing N and H, this approximation is very good.

Let us consider an arbitrary curved quadrangle ABCD (Figure 4) with the vertices

$$A(\theta_{i,k}, q_{mi,k}), \quad B(\theta_{i+1,k}, q_{mi+1,k})$$
$$C(\theta_{i,k+1}, q_{mi,k+1}), \quad D(\theta_{i+1,k+1}, q_{mi+1,k+1})$$

The reverse transformation equations using the linear quadrangle approximation can be obtained through very simple mathematical operations as

$$\left.\begin{aligned}
\theta &= \frac{b\xi - a + (c\xi + K_{1i,k})(e\eta - d)}{1 - (c\xi + K_{1i,k})(f\eta + K_{1i,k})} = \theta(\xi, \eta) \\
q_m &= \frac{e\eta - d + (f\eta + K_{1i,k})(b\xi - a)}{1 - (c\xi + K_{1i,k})(f\eta + K_{1i,k})} = q_m(\xi, \eta)
\end{aligned}\right\} \qquad (21)$$

where

11

$$\begin{aligned}
&a = K_{11,k}q_{m1,k} - \theta_{1,k}, \quad b = \Delta\theta + K_{11,k}q_{m1,k} - K_{11,k+1}q_{m1,k+1} \\
&c = -K_{11,k} + K_{11,k+1}, \quad d = K_{1,k}\theta_{1,k} - q_{m1,k} \\
&e = \Delta q_m + K_{1,k}\theta_{1,k} - K_{i+1,k}\theta_{i+1,k}, \quad f = K_{i+1,k} - K_{1,k} \\
&\Delta\theta = \theta_{1,k+1} - \theta_{1,k}, \quad \Delta q_m = q_{m1+1,k} - q_{m1,k} \\
&K_{1,k} = \frac{q_{m1,k+1} - q_{m1,k}}{\theta_{1,k+1} - \theta_{1,k}}, \quad K_{i+1,k} = \frac{q_{m1+1,k+1} - q_{m1+1,k}}{\theta_{i+1,k+1} - \theta_{i+1,k}} \\
&K_{11,k} = \frac{\theta_{i+1,k} - \theta_{1,k}}{q_{m1+1,k} - q_{m1,k}}, \quad K_{11,k+1} = \frac{\theta_{i+1,k+1} - \theta_{1,k+1}}{q_{m1+1,k+1} - q_{m1,k+1}}
\end{aligned}$$
$$\tag{22}$$

Thus, after ξ_G and η_G are known, we can use equation (21) to
directly obtain θ_G and q_{mG}. The results of numerical calcula-
tion (shown later) indicate that this method almost has the
same precision as the "accurate" reverse transformation. How-
ever, the calculation time can be drastically reduced. It is
even possible to reduce the computation time by 1/3.

3. Simplified Uni-directional Sampling Approximation

In our earlier computation process, we have used another
simple approximation method which considers the reverse trans-
formation approximately as

$$\theta = \theta(\xi), \quad q_m = q_m(\eta) \tag{24}$$

Therefore, we can use the uni-direction sample strip inter-
polation method to obtain the values of $\theta_{Gi,k}$ and $q_{mG,i,k}$ from
$(\xi_{Gi,k}, \eta_{G,i,k})$. This approximation method is very simple but its
accuracy is relatively poor.

After the reverse transformation is obtained, we can pro-
ceed with the same steps which follow as in Reference [1].
The iteration continues with the maximum momentum variation
max at the new streamline point is less than the given accuracy
ε_{max}. The actual details of program compilation are omitted here.

12

IV. Calculated Examples and Analysis

We have used the above method to compile the 719 computer program of our school and carried out an numerical calculation on the modified centrifugal compressor turbine of the GJ11# pressure riser of Shanghai Diesel Engine Factory. The calculation regime is: inlet temperature T_1 = 293°K, inlet specific gravity $\gamma_1 = 1.1695 \text{kg/m}^3$, isobaric specific heat $C_p = 1022.33 \text{kg} \cdot \text{m/kg} \cdot °K$, variational coefficient n_0 = 1.506, mass flux C_0 = 0.3 kg/s, angular velocity $\omega = 4188.8 \text{rad/s}$, number of blades Z_N = 14, number of quasi-orthogonal surfaces m = 13, number of S_1 surfaces $N + 1$ = 9, number of S_2 surfaces $H + 1$ = 9.

Since the calculated data are too much to show, we are only going to present part of the data showing the major relevant results. Figure 5 shows the meridional surface lines of the turbine and the meridional line of the S_2 surfaces. Figure 6 gives the distribution of relative Mach number on the average S_2 surface (k = 5) and also shows the comparison of the distribution of M using the revolving surface assumption with our results when $k = 5, j = 1, 5, 9$ (notice that the $\overline{m}$ coordinate in the figure, one uses the percentage of the arc length of the meridional streamline and the other uses the percentage of the arc length of spatial streamline). Figures 7 – 9 show the distribution of M and the diagrams of streamline of the cross blade spatial streamlines when j = 1, 5, 9. Figure 10 indicates the twisting condition of the intersection between the quasi-orthogonal surfaces S_1 and S_2 when i = 1, 5, 9, 13. It also simultaneously gives a comparison between of the results of calculation obtained using the revolving surface assumption at the inlet surface (i = 1) and those using the method described in this paper. It only shows the deviation of the S_1 surfaces. Figure 11 shows the comparison of results obtained using the three reverse transformation methods on the calculation of the

twisting of the S_1 surfaces (only $i = 1$ is plotted). Figure 12 shows the condition of S_1 surface twisting when the number of blades $Z_N = 18$.

From these calculated examples, we can see the following:

1. From Figures 6 - 9, it was found that the results obtained using the method in this paper is basically similar to those obtained using the method described in Reference [1]. From Figures 10 and 12, it was found that the relative twisting of the surfaces is relatively small, approximately 3 - 10%. Therefore, the results obtained using the revolving surface assumption and non-revolving surface method are very close. Therefore, in general, the revolving surface assumption is still applicable.

2. From Figure 10, we can see that the present calculated shapes of the S_1 surfaces sometimes appear to be slightly convex (the surface of $J = 3$ is most apparent). The height at both ends varies with $i - 1$, 5, 9, 13 differently. At the inlet ($i = 1$) the pressure surface q_m is higher than the suction surface. This phenomenon is consistent with the results obtained from the two-dimensional simplification of the axi-symmetrical flow machinery. At the front middle part of the centrifugal turbine ($i = 5$), the S_1 surface still shows the phenomenon of being slightly convex. The interseting point q_m on the pressure surface, however, is lower than that on the suction surface. Therefore, the surface shows a reverse buckling (twisting) phenomenon. Further back, at $i = 9$, 13 (outlet), another reverse twisting effect appears which causes that the q_m on the pressure surface to behigher than that on the suction surface on the S_1 surface. This phenomenon is not consistent with the result obtained in the two-dimensional simplified calculation of the axial flow machinery. As for whether this belongs to the special

14

Figure 5. Key: 1. inlet
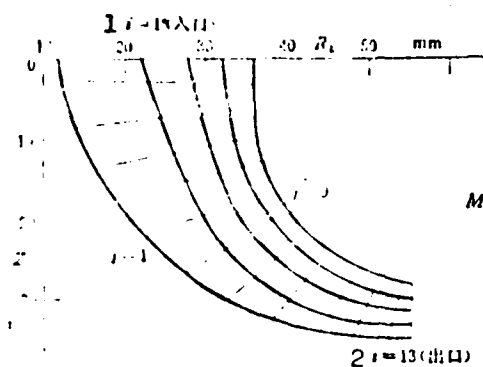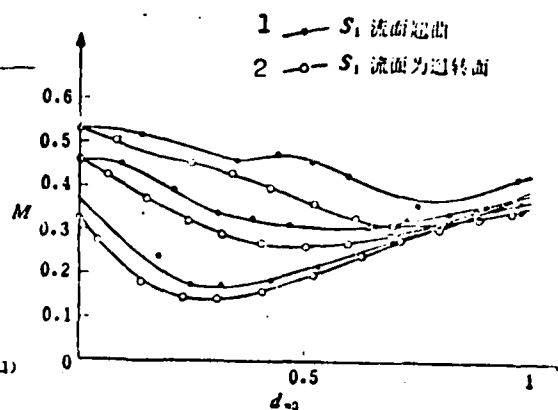2. outlet

Figure 6. Key: 1. S_1 surface
twisted, 2. S_1 surface is a
revolving surface.
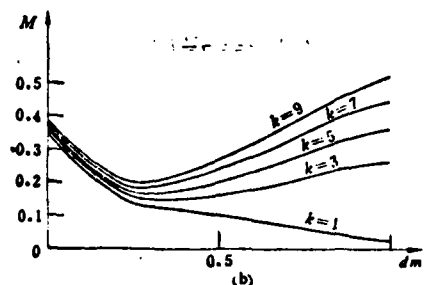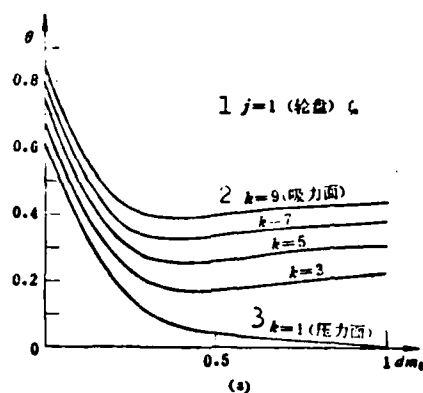

Figure 7

Key: 1. $j = 1$ rotating disc, 2. $k = 9$ suction surface,
3. $k = 1$ pressure surface
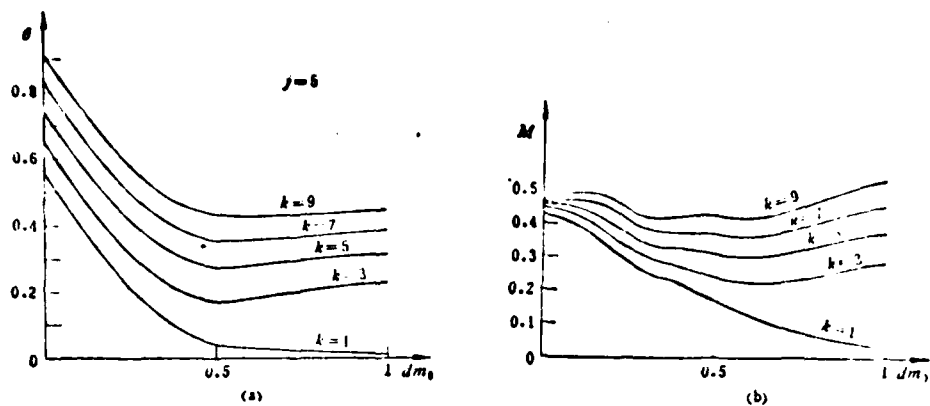
Figure 8
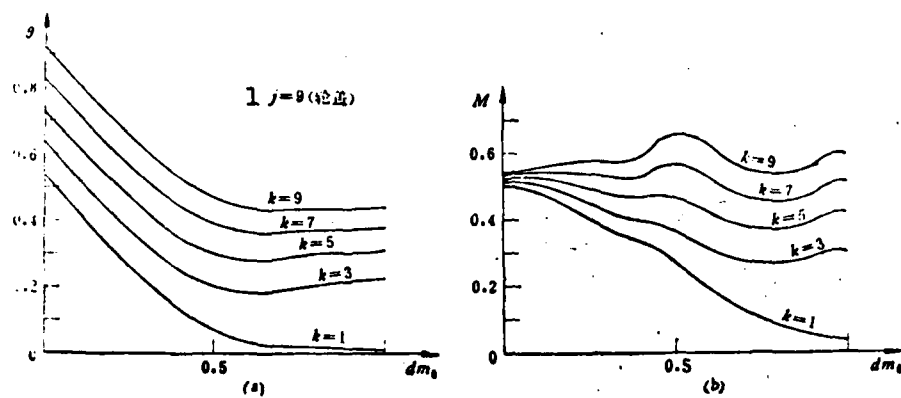
Figure 9.

Key: 1. j = 9 rotating cover
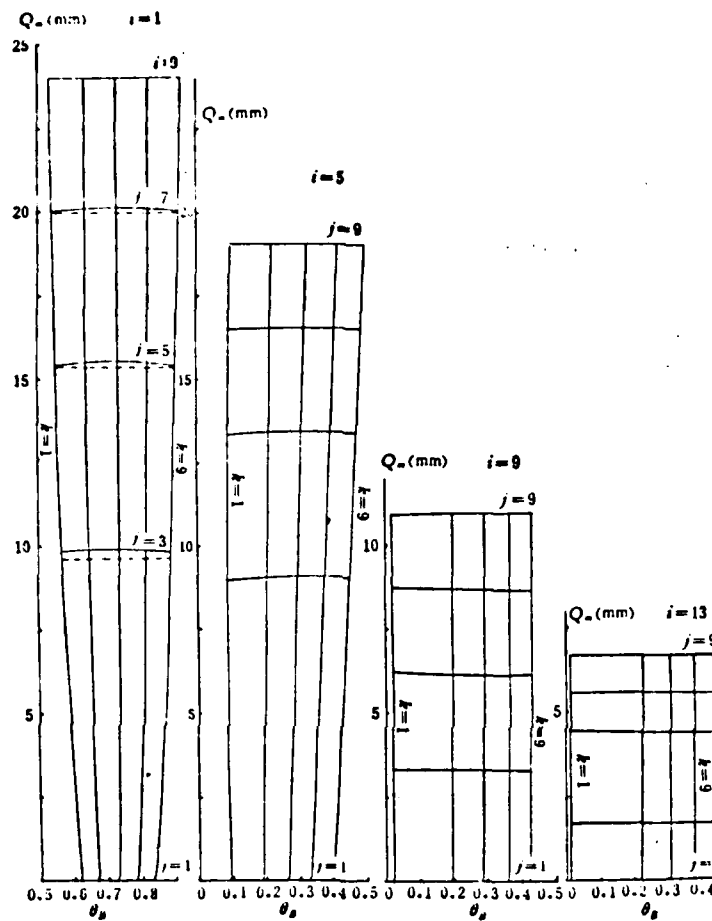
Figure 10

Key: 1. ----- is the result obtained using the assumption that S_1 surface is a revolving surface
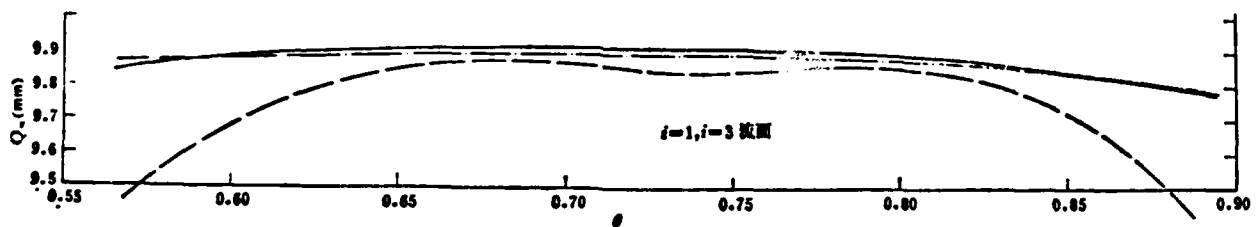
Figure 11

Key: 1. i=1, i=3 surface

17
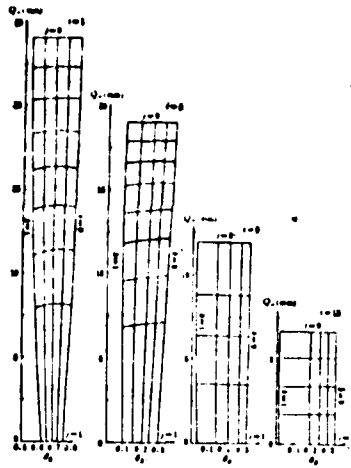
Figure 12

characteristics of the centrifugal machinery, it is still yet
to be verified.

3. From Figure 11, it was found that the linear quadrangle
approximation seems to have the same accuracy as the "accurate"
iterative reverse transformation method. The relative errors
is about 0.5%. The advantage of the linear quadrangle approxi-
mation method is the reduction of calculation time by 1/3. For
example, when the convergence accuracy ε_{max} = 1 mm, both methods
require 16 iterations while the calculation time can be reduced
from 138 to 93 minutes. Therefore, the use of the linear quad-
rangle approximation is reliable and time saving. The use of
uni-directional sampling approximation has a larger error.
The maximum relative error is about 2%.

4. Figure 12 shows the calculated results when max <
10^{-5}m. At this time the maximum momentum variation of Mach
number is 3 x 10^{-4}. This can be considered to be convergent.
But the calculation time is too long.

V. Conclusions

This paper uses an equi-parameter transformation to further develop the procedures mentioned in Reference [1] in order to calculate the three dimensional flow field in the blade channel for an inviscous fluid. The condition of twisting of the S_1 and S_2 surfaces can also be quantitatively determined simultaneously. Based on the results from one turbine, it is reliable. But due to the lack of experimental data and analytic solutions, there is no way to reach certain conclusions for some phenomena and results (such as the small degree of twisting of the surfaces, the double twisting phenomenon, etc.) and it still requires further computational and experimental verifications.

References

[1] Chi Sho Kang and Chiang Chin Lian, Mechanics, 2, (1977).

[2] Stanitz, J. D. & Ellis, G. O., Flow Surfaces in Rotating Axial-Flow Passages, NACA TN-2834 (1952).

[3] Wu, C. H. (吴仲华), A General Theory of Three-Dimensional Flow in Subsonic and Supersonic Turbomachines of Axial, Radial and Mixed Flow Types, NACA TN-2604 (1952).

THE PRINCIPLES AND METHODS FOR SHAPING THE WING ROOT REGIONS OF A
WING-BODY COMBINATION AT TRANSONIC AND LOWER SUPERSONIC SPEEDS[*]

Yang Tso Sheng, Tai Chia Tsun, Ch'en Ching Sung, Fan Chia I
(Nanching Aeronautical Institute)

Abstract

On the basis of the author's previous work[1], this paper deals with the principles and methods for the combined shaping of the wing root regions of a wing-body combination, in accordance with the requirements of area rule and shockless pressure field.

It is shown that the favorable non-midwing arrangement is able to reduce the amount of fuselage shaping required for the reduction of the zero lift wave drag of a wing-body combination. The combined shaping so designed may thus be realized more easily in structual arrangement.

I. INTRODUCTION

In fuselage designs based on the "area rule", there usually still exists the problem of the appearance of shock waves on the wings and the reduction of wave drag to the expected value cannot be achieved. If one requires that the fuselage shaping be such that when the pressure field of the fuselage is added to that of the isolated wing, the resultant pressure distribution in the wing root regions will be congruent with the pressure distribution on the equivalent yawed wing, then shock waves will definitely not appear on the wings. In this manner, the "area rule" can be used to full advantage [1-3]. The fuselage shaping required when such a pressure field method is adopted is generally fairly large. In order to reduce the amount of shaping, one needs to resort to combined shaping, i.e., the wing shape in the wing root regions needs to be appropriately tailored--the wing thickness near the front of

20

the wing root regions has to be increased and the position of max-
imum wing thickness has to be shifted gradually from outside of
the wing root regions towards the wing root regions [4]. In addi-
tion, we have found that if a favorable non-midwing arrangement
is adopted, fuselage shaping can be substantially reduced. We
have given in reference [5] the method for calculating the press-
ure field of the fuselage for a non-midwing arrangement. The
equation derived there will be directly applied in the present
paper.

2. THE AERODYNAMIC DESIGN OF THE WING SECTION AND FILLET IN THE WING ROOT REGIONS

For a given Mach number M in supersonic designs, the wing
section at the wing root for a given pressure distribution can
only be obtained by means of successive approximations. Such a
procedure is tedious. The key to achieving faster convergence lies
in choosing correctly the wing section in the wing root regions in
the first approximation.

1. Determination of wing section in the wing root regions in the first approximation

We simplify the problem by considering an infinite swept-back
wing of constant chord. The sweep angle Λ is equal to the sweep-
back of the minimum pressure isobar of the equivalent yawed wing.
The relation between the linearized pressure coefficient C_p of the
infinite swept-back wing under the conditions of subsonic leading
edge and the slope dz/dx of the wing section has been given in [6]
to be

$$C_p = \left\{\left[\frac{2\cos\Lambda}{\pi\sqrt{1 - M^2\cos^2\Lambda}} \ln\left[\frac{\sqrt{1 - M^2\cos^2\Lambda} + \sin\Lambda}{\sqrt{1 - M^2\cos^2\Lambda} - \sin\Lambda}\right]\right]\right\} \frac{dz}{dx} \qquad (1)$$

There are definite difficulties associated with solving for the shape of the wing section by means of Equation (1) under given pressure distribution on the equivalent infinite yawed wing. This is because for subsonic critical flow, the C_p near the trailing edge of the equivalent infinite yawed wing has to return to a positive value. According to Equation (1), the slope of the wing section should be positive. This causes the wing section to stay open along the trailing edge. Note that in subsonic flow round infinite swept-back wing of constant chord, the pressure distribution on the wing section in the root regions is given by [7,8].

$$C_p = \frac{-2\cos\Lambda}{\sqrt{1 - M^2\cos^2\Lambda}}\left\{\frac{1}{\pi}\int_0^1 \frac{\frac{dz}{dx}\,dx'}{x - x'} - \frac{1}{\pi}\ln\left[\frac{\sqrt{1 - M^2\cos^2\Lambda} + \sin\Lambda}{\sqrt{1 - M^2\cos^2\Lambda} - \sin\Lambda}\right]\frac{dz}{dx}\right\} \tag{2}$$

Comparing Equations (1) and (2), one sees that the second term in Equation (2) is nothing but the pressure coefficient of the wing section in the root region under conditions of supersonic flow round an object (the leading edge of subsonic flow). Its weight in Equation (2) increases with the M number of the oncoming flow. Hence, we make the pressure distribution under higher subsonic M numbers (e.g., M = 0.9) equal to that of the corresponding equivallent infinite yawed wing in accordance with Equation (2). The wing section in the root regions thus determined not only results in improved pressure distribution on the wing section in the root region under transonic flows, but also causes the pressure distribution of the wing section in the root region to converge to that of its corresponding infinite yawed wing under lower supersonic flows. Therefore, it is reasonable to use this as a first approximation to the shape of the wing section in the root region for a given M number in supersonic designs. We express the integral and dz/dx in Equation (2) in terms of sums of the ordinate z of the wing section:

$$C_p(x_\nu) = -\frac{2\cos\Lambda}{\sqrt{1-M^2\cos^2\Lambda}}\left[\sum_{\mu=1}^{N-1} s^{(1)}_{\mu\nu}z_\mu - f(\Lambda)\sum_{\mu=1}^{N-1} s^{(2)}_{\mu\nu}z_\mu\right] \tag{3}$$

In which

$$f(\Lambda) = \frac{1}{\pi}\ln\left|\frac{\sqrt{1-M^2\cos^2\Lambda}+\sin\Lambda}{\sqrt{1-M^2\cos^2\Lambda}-\sin\Lambda}\right| \qquad (\nu=1,2,\cdots,N-1) \tag{4}$$

Thus, for a given pressure distribution on the wing root wing section, one can solve from Equation (3) the ordinate z_μ corresponding to any specific x_μ. Here, x_μ and z_μ are dimensionless quantities. The characteristic length used for conversion into dimensionless quantities is the wing root chord c_o. In this set of equations, N is the number of terms in the sums. Value for x_ν, $s^{(1)}_{\mu\nu}$ and $s^{(2)}_{\mu\nu}$ corresponding to x_ν in the cases N = 8,16,32 have been tabulated [7]. Suppose the variation in the wing root wing section will converge at spanwise position Y_2. Take the wing section at that point to be the control wing section. The region between the wing root wing section and the control wing section is called the wing root region. The spanwise variation of the wing section in the wing root region at each point on the lines of constant percentage chord can be regarded as a parabola or a cosine curve. As the entire wing region within the front Mach line of the wing section in the root regions has some effect on the pressure distribution on the wing section in the root regions, one can take the spanwise coordinate of the point of intersection of the said front Mach line and the leading edge of the wing to be Y_2.

Results of calculations for actual examples show that if one makes the pressure distribution on the wing root coincide exactly with that on the equivalent yawed wing, negative values for the ordinate of the wing root wing section will appear near the trailing edge. This means that the upper and lower surfaces of the wing section will meet at some point in front of the trailing edge and not close to the trailing edge. This is not reasonable. Hence, one can only match the pressure distribution on the wing root wing
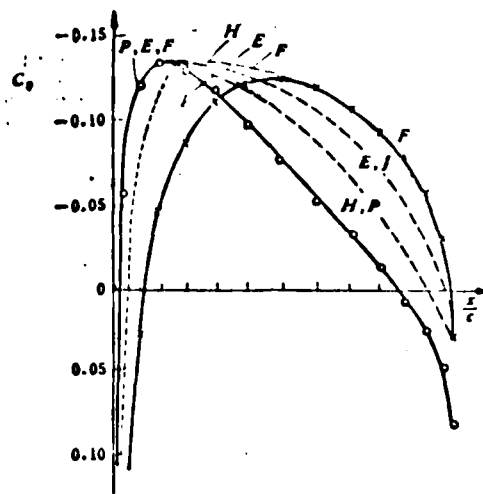
Figure 1.   Chordwise distribution of C_p of wing
root wing section
    o   equivalent yawed wing
    x   original wing root wing section

section to that on the equivalent yawed wing to the largest poss-
ible extent. Our procedure is as follows: 1) Modify the press-
ure distribution before the minimum pressure point of the orig-
inal wing root wing section so that it coincides exactly with
that on the equivalent yawed wing. The pressure distribution
after the minimum pressure point should be between the pressure
distributions of the equivalent yawed wing and the original wing
root wing section, as illustated by curves P, E, F in Figure 1.
2) Make the pressure distribution before and after the minimum
pressure point lie between those of the equivalent yawed wing and
the original wing root wing section, as illustrated by curves H
and J in Figure 1. Under the requirement that the trailing edge
of the wing section should be closed, the closer the pressure dis-
tribution on the wing root wing section is to that on the equi-
valent yawed wing, the further forward will the point of maximum
thickness of the wing root wing section shift. This causes the
entire wing section to reduce in thickness. To overcome this
problem, we note that the point of maximum thickness shifting for-
ward means that the thickness at the leading edge of the wing

section in the root regions needs to be increased. Hence, we can satisfy this requirement without having to move the point of maximum thickness of wing section excessively forward by extending the chord of the wing section in the root regions, i.e., by adding a fillet to the wing root region.

2. The aerodynamic design of the wing root region fillet in the first approximation

Consider a trapezoidal swept-back wing. Suppse the position of the point of minimum pressure on the first approximation wing root wing section has already been shifted from point C on the original wing root wing section to point B. Since point B still
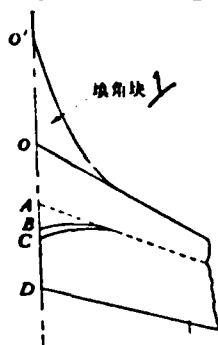
Figure 2
Key: 1--fillet

falls behind the point of minimum pressure A of the equivalent yawed wing (Figure 2), one needs to employ the method of lengthening the chord of wing root to make the point of minimum pressure of the wing root wing section fall on point A. Let the distance between point B and the leading edge be OB, and denote its ratio to the original chord OD as x_1, i.e., $x_1 = $ OB/OD. If the chord of the wing root wing section is extended to O' such that the point of miminum pressure falls on point A, then since $x_1 = \dfrac{O'A}{O'D} = \dfrac{OB}{OD}$ and OA $=$ OD$\cdot x_o$, where x_o is the ratio of the distance OA between the point of minimum pressure of the equivalent yawed wing and the leading edge to the original chord OD, one obtains for the extended chord the expression

$$OD' = \frac{O'A}{x_1} = OD\left(\frac{x_o - 1}{x_1 - 1}\right) \cdot \tag{5}$$

To determine the spanwise shape of the leading edge of the wing root region fillet, one needs to determine the spanwise variation

of the position of the point of minimum pressure in the wing root
section. Then, in accordance with the requirement that the line
joining the points of minimum pressure on all the wing sections
of the wing root regions should coincide with that joining the
points of minimum pressure on the equivalent yawed wing, the
amount of chord lengthening required for each wing section of the
wing root regions can be determined in the manner described above.
Thus, the shape of the leading edge of the fillet in the first
approximation can be determined.

Numerical procedures are generally required for determining
the pressure distribution on each wing section in the wing root
regions. For the design of the shape of the fillet in the first
approximation, one can employ the method suggested in [9], multiply
K_3 with the first term, and K_2 with the second term on the right
hand side of Equation (3), and obtain

$$C_p(x_v) = -\frac{2\cos\Lambda_t}{\sqrt{1-M^2\cos^2\Lambda_t}}\left[\sum_{r=1}^{N-1} K_3 s_{x,v}^{(1)} z_r - K_2 f(\Lambda_t)\sum_{r=1}^{N-1} s_{x,v}^{(2)} z_r\right] \tag{6}$$

In the above equation, Λ_t is the sweep-back of the line joining
points of constant x_v in the wing root regions. $K_2 = 1$ at the
wing root and decreases along the spanwise direction. For its
values, see Figure 1 of [10]. For the values of K_3, see Equations
(10) and (11) of [10].

3. ZERO-LIFT SHAPING FOR THE FUSELAGE NEAR THE WING-FUSELAGE
   JUNCTION FOR A GIVEN M NUMBER IN SUPERSONIC DESIGNS

After the calculations in the first approximation have been
made, the pressure distribution and fuselage shaping should be
computed according to the linearized supersonic theory for the
three-dimensional wing. If the fuselage shaping is still too
excessive, then the wing section in the wing root regions obtained
in the first approximation has to be modified. The position of

maximum thickness of the wing section in the root regions should
be shifted forward to beyond 15% of the chord and, if necessary,
to 6.5% of the chord. The ratio of the maximum thickness of the
wing section to the chord should be approximately increased so as
to obtain a smooth variation along the chord for the slope of the
modified new wing section. The pressure distribution and fuselage
shaping should be again computed. The process is repeated until
the results converge to what is desired.

For a swept-back wing-body combination, when the ratio of
the wing root chord to the radius of the fuselage is greater than
6, the pressure distribution due to thickness on the wing of the
combination is basically similar to those on the isolated wing
obtained by regarding the side of the fuselage as a reflecting
plane. Of course, there are definite differences between the two
in the wing section of the root regions, especially in the rear
part of the root chord. But this will not cause any appreciable
error in the design [1]. Hence, one can regard the pressure dis-
tribution due to thickness on the wing obtained after fuselage
shaping to be approximately equal to the sum of the pressure dis-
tribution on the wing resulting from fuselage shaping. The amount
of fuselage shaping is determined from the difference between the
pressure distribution due to thickness on the wing and that on the
required equivalent yawed wing. Hence, one should first calculate
the pressure distribution due to thickness on the isolated wing.
Then calculate the pressure distribution resulting from the fuse-
lage shaping and then calculate the amount of fuselage shaping
required.

1. Calculation of pressure distributions due to thickness
   of the supersonic isolated wing

Consider a thin wing. The pressure coefficient due to thick-
ness at the singular point on the wing plane ($z = 0$) has been cal-
culated to be [11]

$$C_p(X, Y, 0) = -\frac{2}{\pi}\int_{\beta_1}^{\beta_1}\int_0^{\alpha^*}\frac{(\alpha_1 - \alpha)f(\alpha,\beta)d\alpha\, d\beta}{\bar{c}(\beta)\alpha^{1/2}(\alpha_1 - \alpha_2 - \alpha)^{1/2}(\alpha_1 + \alpha_2 - \alpha)^{1/2}}$$

$$+ \frac{1}{B + \lg \Lambda_{01}}\left[\frac{R_0(\beta_1)}{x - sx_1^*(\beta_1)}\right]^{\frac{1}{2}} + \frac{1}{B + \lg \Lambda_{02}}\left[\frac{R_0(\beta_2)}{x - sx_1^*(\beta_1)}\right]^{\frac{1}{2}} \qquad (7)$$

In the above equation $(X,Y,0)$ and (α,β) denote the dimensionless quantities corresponding to the stationary point $(x,y,0)$ and the moving point (ξ,η) respectively:

$$X = \frac{x - sx_1^*(Y)}{s\bar{c}(Y)}, \quad Y = \frac{y}{s}; \quad \alpha = \frac{\xi - sx_1^*(\beta)}{s\bar{c}(\beta)}, \quad \beta = \frac{\eta}{s}$$

After this coordinate transformation, the front Mach line equation $\xi = x \pm B(\eta - y)$ for point $(x,y,0)$ on the $z = 0$ plane becomes

$$\alpha = \alpha_1 \pm \alpha_2, \quad \alpha_1 = \frac{1}{\bar{c}(\beta)}\,[X\bar{c}(Y) + x_1^*(Y) - x_1^*(\beta)], \quad \alpha_2 = \frac{B(\beta - Y)}{\bar{c}(\beta)},$$

x_1^* denotes the dimensionless quantity corresponding to the coordinate $x_1^* = x_1/s$; $\bar{c}$ denotes the dimensionless quantity corresponding to the wing section chord, $\bar{c} = c/s$; s denotes the half-span of the wing; $R_0(\beta_1)$ and $R_0(\beta_2)$ denote the radius of the wing leading edge at β_1 and β_2, respectively; Λ_{o1} and Λ_{o2} denote the sweep-back of the wing leading edge at β_1 and β_2, respectively, where β_1 is the β coordinate of the point of intersection of the right front Mach line $\alpha = \alpha_1 - \alpha_2$ of the fixed point $(x,y,0)$ and the right leading edge, and β_2 is the β coordinate of the point of intersection of the left front Mach line $\alpha = \alpha_1 + \alpha_2$ of the fixed point $(x,y,0)$ and the left leading edge; $f(\alpha,\beta)$ is the wing surface slope function at point (α,β), $f(\alpha, \beta) = \frac{\partial z(\xi, \eta)}{\partial \xi}\alpha^{\frac{1}{2}}; B = \sqrt{M^2 - 1}.$

For a subsonic leading edge and a supersonic trailing edge, the domain of integration for Equation (7) can be divided into three regions, as shown in Figure 3. For region (1), $\alpha^* = \alpha_1 - \alpha_2$; for regions (2) and (5), $\alpha^* = \alpha_1 + \alpha_2$. Thus Equation (7) can be rewritten as

$$C_p = \frac{2}{\pi}\left[-\int_Y^{\beta_i} \int_0^{\alpha_i - \alpha_i} A\,d\alpha\,d\beta - \int_0^Y \int_0^{\alpha_i + \alpha_i} A\,d\alpha\,d\beta - \int_{\beta_i}^0 \int_0^{\alpha_i + \alpha_i} A\,d\alpha\,d\beta \right]$$

$$+ \frac{1}{B + \lg \Lambda_{0i}}\left[\frac{R_0(\beta_1)}{x - sx_i^0(\beta_1)}\right]^{\ddagger} + \frac{1}{B + \lg \Lambda_{0i}}\left[\frac{R_0(\beta_1)}{x - sx_i^0(\beta_1)}\right]^{\ddagger} \qquad (8)$$

in which $A = \dfrac{(\alpha_1 - \alpha)f(\alpha, \beta)}{c(\beta)\tau^{1/2}(\alpha_1 - \alpha_2 - \alpha)^{1/2}(\alpha_1 + \alpha_2 - \alpha)^{1/2}}$, and $\oint$ denotes the finite portion of the integral.

As the integrand A in Equation (8) contains a singularity at $\alpha = 0$ (leading edge) and another one at $\alpha = \alpha_1 + \alpha_2$ (on the front Mach line), these singularities have to be removed before numerical integration can be performed. For integrals containing square-root singularities, such as

$$\int_0^{\alpha_i - \alpha_i} \frac{d\alpha}{\alpha^{1/2}(\alpha_1 - \alpha_2 - \alpha)^{1/2}},$$

we can make the following variable substitution:
Let $\alpha = 0.25(\alpha_1 - \alpha_2)(1 + \zeta)^2(2 - \zeta)$,   . The integral then becomes
$\int_{-1}^{1} \dfrac{3d\zeta}{(4 - \zeta^2)^{1/2}}$,   in which the integrand is positive everywhere with the range of integration. After this treatment, no more singularities exist in the integrals in Equation (8) and the Gaussian method can be applied in the numerical integration.
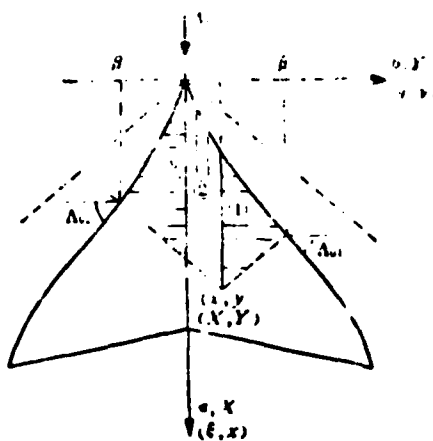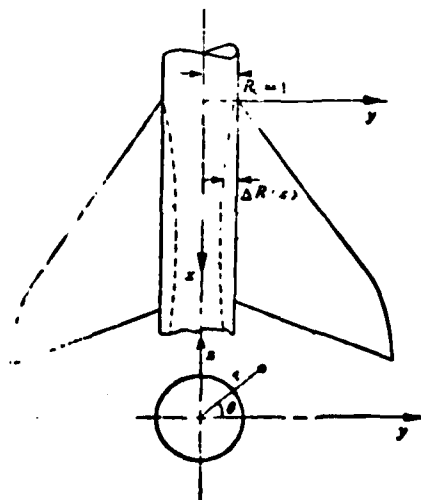

Figure 3   Figure 4

Let the equation for symmetrical fuselage shaping be

$$\frac{\partial R}{\partial x} = t \sum_{n=0}^{\infty} g_{2n}(x) \cos 2n\theta \tag{9}$$

For a mid-wing arrangement, the pressure distribution on the wing
and the fuselage caused by symmetrical fuselage shaping is given
by [12,13]. (Let $B = \sqrt{M^2 - 1}$)

$$C_{p,w}(x) = \frac{2t}{B} \sum_{n=0}^{\infty} \cos 2n\theta \left[g_{2n}(x) - \frac{1}{B} \int_0^x g_{2n}(\xi) W_{2n}\left(\frac{x-\xi}{B}, 1, \cdot\right) d\xi \right] \tag{10}$$

$$C_{p,u}(x) = \frac{2t}{B} \sum_{n=0}^{\infty} \left[\frac{g_{2n}(x - Br + B)}{\sqrt{r}} \right.$$
$$\left. - \frac{1}{B} \int_0^{x-Br+B} g_{2n}(\xi) W_{2n}\left(\frac{x}{B} - r + 1 - \frac{\xi}{B}, r\right) d\xi \right] \tag{11}$$

In the above equations, all the lengths have been divided by the
radius R_0 of the cylindrical section of the unwaisted fuselage;
the x-axis lies along the axis of the fuselage, the y-axis passes
through the point where waisting begins and (x,r,θ) form a cylin-
drical coordinate system (see Figure 4); R is the radius of the
fuselage after waisting; t is a specific parameter, usually taken
as the relative thickness of the wing root wing section; g_{2n} is
the amplitude of fuselage shaping; W_{2n} is the set of special func-
tions associated with the boundary value problem of solving the
wave equation; see [14]. For a symmetrical fuselage, we may set
n = 0 in Equations (10), (11). Then setting r = 1 will give the
pressure distribution on the wing root wing section produced by
the fuselage shaping.

Non-midwing arrangement is an important measure for reducing
fuselage shaping. We have in [5] found the additional pressure

distribution on the wing root wing section due to the non-midwing
arrangement in the case of axially symmetrical fuselage shaping
to be

$$\Delta C_p(x) = -\frac{1}{\pi}\left\{ F\frac{d^2R}{dx^2} + N\frac{dR}{dx}\right\} = -\frac{\iota}{\pi}\left\{ F\frac{d\iota}{dx} + \cdots \right\}$$ (12)

See Equation (39) in [5] for the definition of the functions F and
N. Hence, the pressure distribution produced by axially symmetric
fuselage shaping on the wing root wing section in a non-midwing
arrangement will be given by

$$C_{p\text{ non-m}}(x) = C_{p\text{ m}}(x) + \Delta C_p(x) = \frac{2\iota}{B}\left[g_0(x) \right.$$

$$\left. -\frac{1}{B}\int_0^x g_0(\xi)W_d\left(\frac{x-\xi}{B},1\right)d\xi \right] - \frac{\iota}{\pi}\left[F\frac{dg_0}{dx} + Ng_0\right]$$ (13)

Key: 1--non-midwing; 2--midwing

3. The design of fuselage shaping near the junction of the wing and fuselage

If the required pressure distribution on the wing root wing
section is $C_{p_r}(x)$, the wing root wing section pressure distribu-
tion for unwaisted fuselage is $C_{p_1}(x)$, and the pressure distribu-
tion on the cylindrical section of the fuselage due to the effect
of the forebody is $C_{p_1}(x)$, , then we require that the pressure dis-
tribution after axially symmetric fuselage shaping be
$C_p(x) = C_{p_r}(x) - C_{p_1}(x) - C_{p_1}(x).$ For a non-midwing arrangement, this
is just the value of C_p on the left hand side of Equation (13)
and Equation (13) is an integral equation involving $g_0(x)$ which
can be solved by numerical integration using the trapezoidal for-
mula. If we take the interval to be δ, then when $x = m\delta$, by
setting $\left(\frac{dg_0(x)}{dx}\right)_{x=m\delta} = \frac{g_0(m\delta) - g_0(\overline{m-1}\delta)}{\delta}$, one obtains from Equation
(13)

$$g_o(m\delta) = \left[\frac{B}{2\iota}C_p(m\delta) + \frac{\delta}{B}\left\{\frac{1}{2}g_o(0)W_o\left(\frac{m\delta}{B},1\right) + \cdots + g_o(\overline{m-1\delta})W_o\left(\frac{\delta}{B},1\right)\right\}\right.$$
$$\left. - \frac{B}{2\pi\delta}F_g(\overline{m-1\delta})\right]\bigg/\left[1 - \frac{\delta}{2B}W_o(0,1) - \frac{B}{2\pi\delta}(F+N\delta)\right] \quad (14)$$

In the above equation, $g_o(0)$ can be determined from Equation (13) to be

$$g_o(0) = C_p(0)\bigg/\iota\left(\frac{2}{B} - \frac{N}{\pi}\right) \quad (15)$$

In the case of a midwing arrangement, let $F = N = 0$ in Equations (14) and (15). After obtaining the value for $g_o(m\delta)$, we integrate Equation (9) for the condition that $n = 0$ by means of the trapezoidal formula by an approximation and obtain the radius of the waisted fuselage.

$$R(m\delta) = 1 + \iota\int_0^{x=m\delta} g_o(\xi)d\xi$$
$$= 1 + \iota\delta\left\{\frac{1}{2}[g_o(0) + g_o(m\delta)] + g_o(\delta) + g_o(2\delta) + \cdots + g_o(\overline{m-1\delta})\right\} \quad (16)$$

If we require that the fuselage be smooth where the wing-fuselage junction commences, i.e., that $\left.\frac{\partial R}{\partial x}\right|_{x=0} = g_o(0) = 0$, then we see from Equation (15) that we must have $C_p(0) = 0$ at $x = 0$. If, in addition, we require the axial cross-section area distribution satisfy the "area rule", then the fuselage shaping will not be axially symmetric. Assume the fuselage shaping equation to be

$$\frac{\partial R}{\partial x} = \iota\sum_{n=0}^{\infty} g_{1n}(x)\cos 2n\theta \quad (17)$$

and the area distribution demanded by "area rule" to be $S(x)$. Then (see Figure 5).

From Equation (18) one obtains

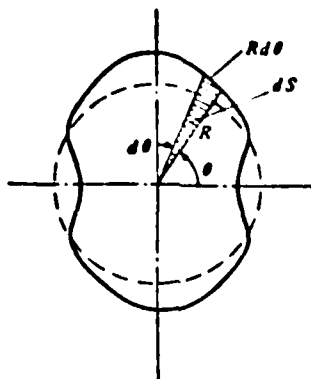$$g_o(x) = \frac{1}{2\pi\iota}\frac{dS}{dx} = M(x) \quad (19)$$

Figure 5

$$S(x) = \int_0^{2\pi} \frac{1}{2} R \cdot R d\theta = \frac{1}{2} \int_0^{2\pi} R^2 d\theta$$

$$\frac{dS}{dx} = \int_0^{2\pi} R \frac{\partial R}{\partial x} d\theta = \int_0^{2\pi} [1 + O(t)] \frac{\partial R}{\partial x} d\theta$$

$$= t \sum_{n=0}^{1} g_{2n}(x) \int_0^{2\pi} \cos 2n\theta d\theta + O(t^2) = 2\pi t g_0(x) + O(t^2) \tag{18}$$

Suppose the pressure distribution produced by fuselage shaping as required by the wing root wing section is $t(C_{po}(x)$; then from Equations (11) and (12), we obtain (considering that ΔC_p is approximately also applicable in the axially symmetrical case)

$$tC_{p_0}(x) = \frac{2t}{B} \Big[g_0(x) - \frac{1}{B} \int_0^x g_0(\xi) W_0 \Big(\frac{x-\xi}{B}, 1 \Big) d\xi + g_2(x)$$
$$- \frac{1}{B} \int_0^x g_2(\xi) W_2 \Big(\frac{x-\xi}{B}, 1 \Big) d\xi \Big] - \frac{t}{\pi} \Big\{ F \frac{dg_0}{dx} + N g_0 \Big\} \tag{20}$$

Substituting Equation (19) into the above equation, one obtains

$$g_2(x) - \frac{1}{B} \int_0^x g_2(\xi) W_2 \Big(\frac{x-\xi}{B}, 1 \Big) d\xi = \frac{B}{2} C_{p_0}(x) - M(x)$$
$$+ \frac{1}{B} \int_0^x M(\xi) W_0 \Big(\frac{x-\xi}{B}, 1 \Big) d\xi + \frac{B}{2\pi} \Big\{ F \frac{dM}{dx} + N M(x) \Big\} = P_1(x) \tag{21}$$

in which we let

$$P_1(x) = \frac{B}{2} C_{p_0}(x) - M(x) + \frac{1}{B} \int_0^x M(\xi) W_0 \Big(\frac{x-\xi}{B}, 1 \Big) d\xi$$
$$+ \frac{B}{2\pi} \Big\{ F \frac{dM}{dx} + N M(x) \Big\} \tag{22}$$

The integrals in Equations (21) and (22) can be computed by approximate integration using the trapezoidal formula. After substituting $c_o(x)$ from Equation (19) and $c_2(x)$ determined from Equation (21) into Equation (17), one can obtain the amount of fuselage shaping $\Delta R(x,\theta)$ at different positions x,θ. For the case of a midwing arrangement, let $N = F = 0$ in each of the above equations.

Finally, the fuselage shaping at the wing-fuselage junction must be such that it smoothly connects to the fuselage shaped according to the "area rule" behind the trailing edge of the wing root wing section.

The results of computation for actual examples show that for a given reduction in zero-lift drag, the amount of shaping is smaller for a lower isolated wing arrangement and is smaller than that required for a midwing arrangement. This is easy to comprehend as, in the non-midwing arrangement, the shielding effect of the fuselage on the upper surface of the wing is enhanced, thus augmenting the effect of the fuselage shaping. Hence, non-midwing arrangement is an important measure for reducing the amount of fuselage shaping.

REFERENCES

[1] Lock, R. C. & Bridgewater, J., Theory of aerodynamic design for swept-winged aircraft at transonic and supersonic speeds, Progress in Aeronautical Sciences, 8, Pergamor Press (1967).
[2] Lock, R. C., Aero. Quart., 12 (1961).
[3] Bridgewater, J., Lock, R. C., Theoretical and experimental investigation of wing-body configurations at low supersonic speeds, AGARD-CP71-71 (1971).
[4] Bridgewater, J. & Wilson, K. H., Influence of wing root shaping on the pressure distribution of swept-wing body configurations, A. R. C.—CP1109 (1970).
[5] Chu Hang, Li Hsüeh, 3(1979), 182-190.

[6] Kuchemann, D., *J. R. A. S.*, 61 (1957).

[7] Weber, J., The calculation of the pressure distribution over the surface of two dimensional and swept wings with symmetrical aerofoil sections, A. R. C. —— R & M 2918.

[8] Kuchemann, D. & Weber, J., The subsonic flow pass swept wings at zero lift without & with body, A. R. C. —— R & M 2908.

[9] Haines, A. B., *J. R. A. S.*, 61 (1957).

[10] Method for predicting the pressure distribution on swept wings with subsonic attached flow. Royal Aeronautical Society Transonic Data Memorandum 6312.

[11] Eldrige, R. H., A numerical method for calculating the pressure due to thickness on symmetrical wings at zero incidence in supersonic flow, A. R. C. —— R & M 3535 (1966).

[12] Nilsen, J. N., Quasi-cylindrical theory of wing-body interference at supersonic speeds and comparison with experiments, NACA-TR1252.

[13] Jones, J. G., A method for designing body shape to produce prescribed pressure distribution on wing body combinations at supersonic speeds, A. R. C. —— CP 540.

[14] Nilsen, J. N., Tables of characteristic functions for solving boundary value problems of the wave equation with application to supersonic interference, NACA —— TN 3873.

THE WAVE DIAGRAMS FOR DIFFRACTION AND REFLECTION OF A
TRAVELING WEAK SHOCK WAVE FROM AN OPEN END OF A SHOCK TUBE

Wei Chung Lei, Wang Ping-cheng, Chang Chün Hsiu
(Fui Ching University)

Abstract

The free diffractions of a weak shock wave issuing from an open end of a shock
tube and the formation and development of a vortex ring from the end of the tube
are observed by a schlieren method. Also observed are the oblique reflections from
the horizontal floor and the vertical plate.

As the wave described above impinges on the horizontal surface near grazing
incidence, the Mach stem forms. Under certain conditions, when this Mach stem
travells along a slant surface with an incidence angle which is larger than the critical
value with respect to the horrizontal axis, the phenomena of "dissolution" of the
Mach stem occurs.

The observation of such a new phenomena and its analysis are presented in this
paper.

In 1971, we used a Schlieren method to study the flow dia-
grams of a weak shock wave emitted from a shock tube and the
induced ultra-pressure field. The shock wave inside the tube is
planar and the gas flow velocity in the wake of the wave is in the
subsonic range. After issuing from the opening of the shock tube,
the wave itself is diffracted and undergoes regular reflections
from the horizontal floor and the vertical plate. At the same
time, the gas flow in the wake of the wave forms a vortex ring
outside the tube which travels forward at a definite velocity. In
addition, a sonic emitted flow field is formed near the open end of
the tube. When this shock wave travels along a slanted surface,
one further observes the so-called "dissolution" phenomenon in
which the incident wave and the reflected wave travel separately
along the slanted surface. Such "dissolution" is a new phenomenon
which we will describe and explain on a physical basis in this
paper. Observations have been made on the flow diagrams of waves
issuing from both porous and nonporous tube walls.

1.   WAVE DIAGRAMS

     After the weak shock wave issues from the open end of the
shock tube, it is first diffracted. The corner of the open end
of the tube can be regarded as a source of interfering waves.
Hence, the shock wave will be attenuated by these interfering
waves, and its wavefront changes from a planar to an ellipsoidal
shape when it has traveled a distance equal to the distance of the
tube (plate I, photo 1).

     The main shock wave undergoes regular oblique reflection
from the horizontal floor. Under our experimental conditions, one
can calculate the variation of the intensity of the shock wave with
distance from the tube opening by measuring the angles of incidence
and reflection (plate I, photo 2). One should note that, although
the reflection from the floor is an oblique reflection, its des-
tructive effect is not negligible. Roughly speaking, for medium
strong shock waves, the ultra-pressure in the wake of the reflected
wave is on the same order of magnitude as that of the main
reflected wave. For weak shock waves, it could even exceed the
latter.

     For reflection of the shock wave from a vertical plate placed
at a distance equal to twice the diameter of the tube, the rela-
tion between the angles of incidence and reflection is, on the
whole, that for regular reflection (plate I, photo 3). After the
shock wave is reflected, it suffers from the disturbance from the
vortex ring and the emitted gas flow and is no longer a spherical
wave. Rather, it becomes bow-shaped in the two-dimensional case,
and saucer-shaped in the three-dimensional case. After it passes
through the vortex ring, the main reflected wave increases the
pressure in the original flow region. In the case of a porous
wall, the reflected wave is still saucer-shaped.

In the process of backward movement along the floor of the
incident wave reflected off the vertical plate and the reflected
wave, Mach reflection is sure to occur. The height of the Mach
stem of this Mach reflection (i.e., the height of the fork) in-
creases as the wave moves on, and the intensity of the Mach wave
gradually decreases. Therefore, under the conditions of given
incident wave intensity and given angle of incidence, the height
of the Mach stem can be qualitatively used as a basis for estimat-
ing the attenuation of the Mach wave. Under our experimental con-
ditions, the position of this fork rises with a slope of approx-
imately 15°. The wave diagram for reflection off the vertical
plate is shown in plate I, photos 4 and 5.

For the case where the vertical plate is placed at a distance
equal to twice or four times the tube diameter, the reflection
near the tube is a Mach reflection whether the wall is porous or
not. Experimental results show that, under these conditions, the
destructive effects of the reflected wave on the obstacles and
structures in the vicinity of the wall is obviously larger than
that of the diffracted main shock wave.

2. THE EMITTED GAS FLOW AT THE OPENING OF THE TUBE

Two cases need to be considered for the emitted gas flow, viz.
the case where the flow after the shock wave in the tube is sub-
sonic and the case where it is supersonic.

For the case where the gas flow at the cross-section of the
tube opening is initially subsonic, generally speaking, before
the vortex ring leaves the end of the tube, the divergent waves
arising at the corner of the tube opening will be transmitted into
the tube. This results in increased velocity of the gas flow at
the cross-section of the tube opening, which eventually becomes
sonic. The wavefront of the above mentioned divergent waves have
a stronger thinning effect.

The emitted gas flow following the main shock wave gradually develops from the unaffected trumpet-shaped region into the peach-shaped region as a result of the thinning effect of the divergent waves. This peach-shaped region is where the two divergent waves arising from the corner of the tube opening interfere. It should be pointed out that despite the fact that the main shock wave is continually impinged upon by the divergent waves, as the gas flow emitted from inside the tube keeps on replenishing energy, the ultra-pressure of the shock wave in the vicinity of the central region of the gas flow is actually larger than that in the regions above and below. This is characteristic of the diffraction of the shock wave after issuing from the tube opening.

After the gas flow at the cross-section of the tube opening has been accelerated to sonic velocity by the divergent waves, as the pressure at the tube opening is higher than that outside the tube, the gas flow will continue to be accelerated beyond the tube opening, forming a local supersonic flow region at the tube opening (plate I, photo 6, plate II, photo 7). When the ultra-pressure of emission is 1 kg/cm^2, the Mach number measured for the local supersonic flow for a tube with a nonporous wall is 1.18; while that for a tube with a porous wall is 1.05. Therefore, the Mach number decreases approximately by 11% when the wall is porous.

For the case where the gas flow at the cross-section of the tube opening is supersonic, supersonic emitted flow is formed at the corner of the opening and the divergent waves from the corner will not be able to enter the tube. As the pressure at the tube opening is larger than the atmospheric pressure of the surrounding, the free boundary of the gas flow will certainly expand outward. The flow diagram is similar to that for the stable, constant supersonic emitted flow.

3. THE FORMATION, DEVELOPMENT AND SHATTERING OF THE VORTEX RING

Because of the effect of adhesion, when the gas flows around a pointed corner, a small kernel of vortex ring with a diameter just a little larger than the inner diameter of the tube, is first formed close to the end of the tube. As time goes on, the gas behind the main shock wave keeps feeding the vortex ring. The vortex ring grows fatter and fatter until it finally leaves the tube opening and travels forward at a definite velocity. Because the vortex ring undergoes turbular flow diffusion and momentum exchange with the surrounding gas flow, it further increases in diameter and fatness. However, as a result, the vortex ring becomes looser and looser until it finally falls apart.

After the vortex ring leaves the tube end, it is first accelerated. The velocity reaches a maximum when it has traveled a distance approximately twice the tube diameter. What follows is decelerated motion, shattering and dissipation.

For shock waves driven by high pressure compressed air in a nonporous tube, when the ultra-pressure of emission is 1 kg/cm^2, the average velocity of the vortex ring is 127 m/s; when the ultra-pressure is 4 kg/cm^2, the average velocity of the vortex ring is 156 m/s. For shock waves driven by explosive gas, when the ultra-pressure of emission is 15 kg/cm^2, the average velocity of the vortex ring is 129 m/s.

For shock waves driven by high pressure compressed air in a porous tube, because the emitted shock wave is attenuated, the velocity of the vortex ring is lower by about 10%. In the case of the nonporous tube, the time elapsed before the vortex ring leaves the tube opening is about 250 µs. In the case of the porous tube, the vortex ring leaves the tube opening earlier by about 8%.

4. FLOW DIAGRAM NEAR A POROUS WALL AND THE DISSIPATING EFFECT OF THE PORES

After the main shock wave passes through the pores in the wall, it is emitted out of the pores and diffracted. The waves leaking out of the pores diffuse rapidly and their intensity is rapidly attenuated. At the same time, these waves superpose on one another and form a Mach cone envelope with finite amplitude (plate II, photo 8). The oblique reflection from the floor and the vertical plate of the main diffracted wave has similar wave diagrams for porous and nonporous walls (plate II, photo 9). The pore content of the porous walls discussed in this paper is 1.44% or 2.78%. The pores are uniformly distributed.

What comes after the main shock wave in the tube is a high pressure gas flow. Under the action of this high pressure gas flow the gas particles will certainly be emitted through these small pores into the stationary gas outside of the tube. Hence, a small emitted flow is formed at each pore. When the shock wave is barely emitted from the tube opening, the emitted flow field near the pores has already formed. Approximately at the time the vortex ring is at a distance equal to 1.5 times the tube diameter from the tube opening, owing to the adhesion effect of the gas, the turbulan flow diffusion and momentum exchange among the gas particles in the center region of the emitted flow and those in the surrounding stationary gas result in the merging of the small emitted flow fields at their outer edges.

When the reflected shock wave passes through the emitted flow region at the tube opening and the emitted flow region near the pores, the shock wave will develop two wavefronts (plate II, photo 10).

The waves escaping from the pores can be nothing more than waves with finite amplitudes. It is thus completely reasonable to

assume that these spread out at sonic speeds. Hence, we can deduce the intensity of emission of the main shock wave at the tube opening from the angle of the Mach cone of the envelope of the waves escaping through the pores. The shock wave intensity obtained this way agrees fairly well with that measured with other methods.

The analysis given in Section 1, 2 and 3 shows that the pores in the tube wall can indeed reduce the intensity of the emitted shock wave. Experimental results show that the intensity of the emitted shock wave is less for porous walls than for nonporous walls by about 16% (at the tube opening) and 9% (at a distance 1.8 times the tube diameter from the opening). Qualitatively speaking, we consider the drop to be about 10%.

5. OBSERVATION OF A WEAK SHOCK WAVE TRAVELING ALONG A SLANTED
    SURFACE USING OPTICAL METHODS AND ITS ANALYSIS

When the shock wave emitted from the end of the tube and the wave reflected off the floor travel together along a slanted sur-face, the flow diagrams and the formation of the wave system is very complicated. First, the incident shock wave and the wave reflected off the floor are not planar but are curved. Next, before they hit the slanted surface, they have already formed Mach reflection but with a rather short Mach stem. Furthermore, after they hit the slanted surface, the interfering wave arising from the corner first impinges on the Mach stem and the original re-flected wave. In general, after the Mach stem hits the slanted surface at a definite angle of incidence, reflection of the Mach stem is expected to occur. However, we found in our experiments that in the actual flows the Mach stem "dissolved" and reflection of the original incident wave and that of the wave reflected off the floor occurred separately. This is evident in many of the pictures taken (plate III, photos 13-20).

Now let us explain this phenomenon. First, we analyze the wave diagrams for the case where the Mach stem has been formed before the weak shock wave hits the slanted surface. This is the case for the 30° and 45° slants.

Right after the shock wave hits the corner of the slanted surface, the disturbance of the corner results in the formation of a series of compression waves. As the gas flow behind the shock wave is always subsonic relative to the shock wave, the compression waves will keep impinging on the shock wave. The wavefront of these compression waves is the fan-shaped arc in the photos. As the shock wave is very weak, the reflected wave of the Mach stem merges with the wavefront of the compression waves. Note that the formation and growth of the Mach stem in the Mach reflection is always caused by the incident wave being pushed from the back by the oblique reflected wave. In our case, the slope of rise of this Mach stem is about 15°. Hence, the process of traveling along the 30° and 45° slants is simply the process of reflection of the Mach stem from the slanted surface and that of the shortening of the Mach stem. Those parts of the entire wave (the original incident and reflected waves) that have not been disturbed or reflected by the slanted surface or the corner will continue traveling in the original direction at the original speed. As the waves progress along the slanted surface, the Mach stem is gradually shortened and eventually the fork meets the slanted surface. What follows is the individual reflection and shortening of Mach stem of the incident and reflected waves. The reflected wave of the original wave is tangent to the wavefront of the compression waves issuing from the corner; the reflected wave of the original reflected wave, on the other hand, merges with the wavefront of the compression waves. This is how the Mach stem is "dissolved" and how the original incident and reflected waves separate to be independently reflected and to travel separately along the slanted surface.

[Plate III, photos 13-15 (30° slant); Plate III, photos 16-18 (45° slant)]

For the wave diagrams in which the Mach stem has not been formed before the incident shock wave hits the slanted surface, the process of traveling along the slanted surface is the same as the foregoing, i.e., one in which the incident wave and the reflected wave are separated (plate IV, photos 19-20 (60° slant)). However, for a 15° slant, as the slope of the slanted surface is about the same as that of the rise and growth of the Mach stem, the incident wave and the reflected wave do not separate in the process of traveling along the slanted surface. Here one only observes the impingement of the compression waves on the original shock wave (plate II, photos 11,12).

Thus we see that the wave diagrams for the weak shock wave traveling along a slanted surface depends on the intensity of the wave, the slope of rise of the Mach stem and the fork and also on the slope of the slant itself. To obtain the detailed quantitative relationship among these factors, one needs to make further experimental observations and perform the corresponding numerical calculations.

44
25

END

DATE
FILMED

10-81

DTIC